



AIAA-93-0668

**Recent Developments in High Order K-Exact
Reconstruction on Unstructured Meshes**

Timothy J. Barth
NASA Ames Research Center
Moffett Field, CA 94035-1000

31st Aerospace Sciences Meeting & Exhibit

January 11-14, 1993/Reno, NV

Recent Developments in High Order K-Exact Reconstruction on Unstructured Meshes

Timothy J. Barth

Computational Algorithms and Applications Branch

NASA Ames Research Center

Moffett Field, Ca

§ Abstract

High order accurate solution methods have proven to be invaluable in solving the Euler and Navier-Stokes equations on structured meshes. In this paper we present recent improvements in high order K-exact reconstruction on unstructured meshes. Accurate reconstruction is the key ingredient in obtaining high order spatial accuracy for many upwind finite-volume solvers. The new reconstruction procedures are incorporated into a basic upwind finite-volume scheme suitable for solving scalar advection-diffusion equations as well as the Euler and Navier-Stokes equations. Numerical calculations are performed comparing the present method with lower order accurate reconstruction procedures (piecewise constant and piecewise linear) and various competing technologies such as the fluctuation splitting method of Roe [1] and Deconinck et al. [2] and a system variant of the streamline diffusion Petrov-Galerkin method developed by Hansbo[3] and Hansbo and Johnson [4]. Five test problems are used in the numerical comparisons: scalar circular advection, transonic and supersonic Euler flow, laminar boundary-layer flow, and general compressible Navier-Stokes flow.

§ Introduction

The calculation of Euler and Navier-Stokes flow on unstructured meshes has evolved significantly in recent years. A number of solvers are now available for computing inviscid and/or viscous flow on unstructured meshes, see for example [4-15]. These methods are almost exclusively formulated using linear elements or linear reconstruction. Experience with structured mesh solvers indicates that higher order accurate approximations can significantly improve the quality of numerical solutions. In Barth and Frederickson [16] and Vankeirsbilck and Deconinck [17] high order reconstruction techniques have been developed and implemented within the framework of a finite-volume Euler solver. The relatively high computational cost of these approaches has warranted further research to simplify the overall procedure and reduce the computational cost. The purpose of this paper is to report on recent progress in this area.

§ Preliminaries

Integral Formulation

In the present formulations the integral conservation law form of the Euler and Navier-Stokes equations is solved in a two-dimensional domain Ω with perimeter $\partial\Omega$:

$$\frac{d}{dt} \int_{\Omega} \mathbf{u} dS + \int_{\partial\Omega} \mathbf{F}(\mathbf{u}, \vec{n}) dl = 0 \quad (1.0)$$

In this equation \mathbf{u} is the vector of conserved variables for mass, momentum, and energy. The vector $\mathbf{F}(\mathbf{u}, \vec{n})$ represents the inviscid and viscous flux vector with normal \vec{n} .

Finite-Volume Schemes

In the finite-volume method the solution domain is tessellated into a number of smaller nonoverlapping

subdomains ($\Omega = \cup \Omega_i$). Each subdomain serves as a control volume in which mass, momentum, and energy are conserved. We assume for the present discussions that the solution unknowns are placed at vertices of the mesh and the control volumes are formed from a median dual tessellation of the triangulation as shown in Fig. 1.0.

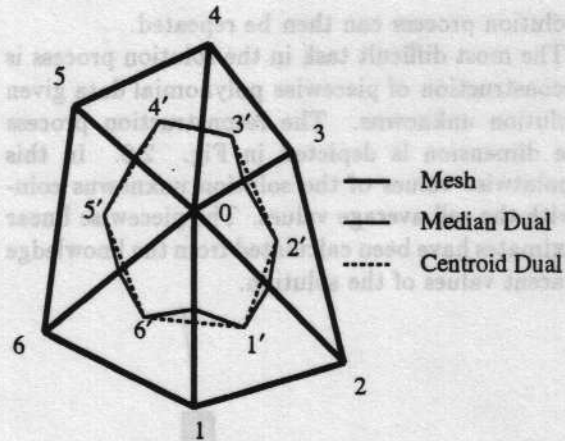


Figure 1.0 Mesh with centroid and median duals.

Note that the use of pointwise values of the solution unknowns is a departure from Godunov's method [18] in which the fundamental unknowns are integral cell averages of the solution in each control volume. This departure significantly changes the "mass" matrix which appears in the discretization of the time integral in Eqn. (1.0). For steady-state calculations the mass matrix can be lumped into a diagonal matrix without sacrificing spatial accuracy. Mass lumping has been used in all calculations presented.

The solution procedure for solving Eqn. (1.0) consists of the following steps:

Reconstruction. Given pointwise values of the solu-

tion at vertices of the mesh, reconstruct a polynomial approximation to the solution in each control volume. These polynomials may vary discontinuously from control volume to control volume.

Flux Quadrature. From the piecewise polynomial description of the solution, approximate the flux integral in Eqn. (1.0) by numerical quadrature. The actual choice of quadrature rule used in the flux integration is dictated by the order of data reconstruction, i.e. one point quadrature formulas with linear reconstruction and two point Gauss quadratures with quadratic reconstruction. Because the piecewise polynomials are discontinuous at control volume boundaries, the Euler flux is supplanted by a numerical flux which is a function of two solution states. Those flux functions which can be characterized as some approximate and/or exact solution of the Riemann problem of gasdynamics result in upwind biased approximations. Roe's approximate Riemann solver [19] is one example of an upwind flux function and will be used in all computations.

Evolution. Given a numerical approximation to the flux integral, evolve the system in time using any class of implicit or explicit schemes. This results in new solution unknowns.

The solution process can then be repeated.

The most difficult task in the solution process is the reconstruction of piecewise polynomial data given the solution unknowns. The reconstruction process in one dimension is depicted in Fig. 2.0. In this case pointwise values of the solution unknowns coincide with the cell average values. The piecewise linear approximates have been calculated from the knowledge of adjacent values of the solution.

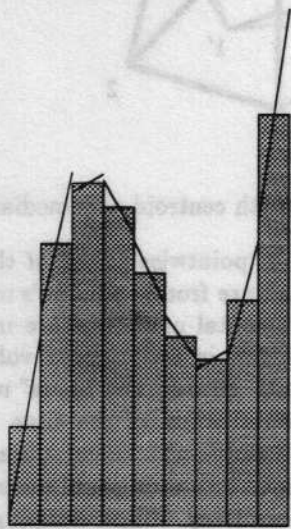


Figure 2.0 Linear reconstruction from cell data.

Unfortunately, advection schemes based on these reconstructed polynomials produce spurious oscillations near discontinuities and regions of high solution gradient unless additional measures are taken. These mea-

asures are the basis for the class of MUSCL schemes developed by van Leer [20,21]. The basic idea is to require that the reconstructed piecewise polynomials do not introduce new maxima or minima into the reconstructed data. The resulting strategy would produce the modified reconstruction shown in Fig. 3.0.

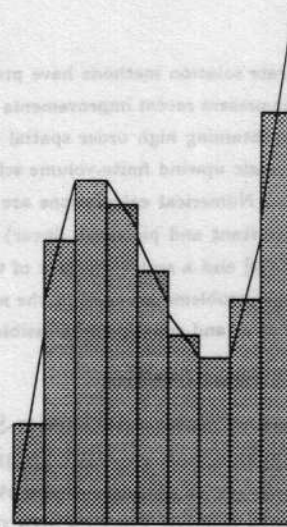


Figure 3.0 Linear reconstruction of data with monotone limiting.

In the next section we present a technique for linear reconstruction on unstructured meshes based on a least-squares principle.

Least-Squares Linear Reconstruction [22]

Given values of the solution at vertices of the mesh, consider two different solution representations obtained from this pointwise data. The first representation is continuous while the second representation is discontinuous. For each triangle a unique linear interpolant exists which passes through the three vertex values. The first representation, $u^{int}(x, y)$, is the C^0 continuous union of these triangle interpolants. The second representation, $u^{recon}(x, y)$, is that polynomial which is to be determined from the reconstruction process for a particular control volume. The reconstructed polynomial in each control volume is determined from the following minimization problem:

Determine the reconstruction polynomial in each control volume which minimizes in L_2 the distance between the two solution representations at all quadrature points used in the flux calculation.

This minimization problem is motivated by the observation that if the continuous interpolant $u^{int}(x, y)$ were actually used in the flux computations then a discretization closely related to the Galerkin finite-element would result. Recall that the Galerkin method produces a solution which is the "best" approximation (in energy) to the actual solution. The minimization problem attempts to find discontinuous reconstruction

polynomials that are close to the C^0 counterparts. For each control volume compute the difference between the two data representations at all quadrature points ($i = 1, 2, 3, \dots, n$) to be used in the numerical flux integration,

$$\overline{\Delta u} = \begin{pmatrix} u_1^{recon} - u_1^{int} \\ u_2^{recon} - u_2^{int} \\ u_3^{recon} - u_3^{int} \\ \vdots \\ u_i^{recon} - u_i^{int} \\ \vdots \end{pmatrix} \quad (2.0)$$

then find the reconstructed vertex gradient which minimizes $\|\overline{\Delta u}\|_2$. For linear reconstruction the flux quadrature points can be placed at edge midsides [5]. Solving the minimization problem is equivalent to solving the following nonsquare matrix problem in a least-squares sense for the control volume surrounding vertex v_0 with incident edges $e(v_0, v_i)$:

$$\begin{bmatrix} \Delta x_1 & \Delta y_1 \\ \Delta x_2 & \Delta y_2 \\ \Delta x_3 & \Delta y_3 \\ \vdots & \vdots \\ \Delta x_i & \Delta y_i \\ \vdots & \vdots \end{bmatrix} \begin{pmatrix} u_x \\ u_y \end{pmatrix} = \begin{pmatrix} (u_1 - u_0) \\ (u_2 - u_0) \\ (u_3 - u_0) \\ \vdots \\ (u_i - u_0) \\ \vdots \end{pmatrix} \quad (3.0)$$

where $\Delta x = x - x_0$ and $\Delta y = y - y_0$. This equation can also be written in symbolic form

$$\begin{bmatrix} \overline{L}_1 & \overline{L}_2 \end{bmatrix} \nabla u = \overline{f}.$$

Exact calculation of reconstruction gradients for linear u is guaranteed if any two row vectors span all of 2-space (this is always true in the present applications). The resulting system is most easily solved via normal equations

$$\begin{bmatrix} L_{11} & L_{12} \\ L_{12} & L_{22} \end{bmatrix} \nabla u = \begin{pmatrix} f_1 \\ f_2 \end{pmatrix} \quad (4.0)$$

where $L_{ij} = (\overline{L}_i \cdot \overline{L}_j)$ and $f_i = (\overline{L}_i \cdot \overline{f})$. In practice the inner product sums L_{ij} and f_i can be calculated by a single loop through all edges of the mesh:

For $k = 1, n(e)$! Loop through edges of mesh

$j_1 = e^{-1}(k, 1)$! Pointer to edge origin

$j_2 = e^{-1}(k, 2)$! Pointer to edge destination

$dx = (x(j_2) - x(j_1))$! Δx

$dy = (y(j_2) - y(j_1))$! Δy

$l_{11}(j_1) = l_{11}(j_1) + dx \cdot dx$! l_{11} origin sum

$l_{11}(j_2) = l_{11}(j_2) + dx \cdot dx$! l_{11} destination sum

$l_{12}(j_1) = l_{12}(j_1) + dx \cdot dy$! l_{12} origin sum

$l_{12}(j_2) = l_{12}(j_2) + dx \cdot dy$! l_{12} destination sum

$l_{22}(j_1) = l_{22}(j_1) + dy \cdot dy$! l_{22} origin sum

$l_{22}(j_2) = l_{22}(j_2) + dy \cdot dy$! l_{22} destination sum

$du = (u(j_2) - u(j_1))$! Δu

$f_1(j_1) = f_1(j_1) + dx \cdot du$! f_1 origin sum

$f_1(j_2) = f_1(j_2) + dx \cdot du$! f_1 destination sum

$f_2(j_1) = f_2(j_1) + dy \cdot du$! f_2 origin sum

$f_2(j_2) = f_2(j_2) + dy \cdot du$! f_2 destination sum

Endfor

From these inner product sums reconstructed gradients are obtained from the 2×2 system given in Eqn. (4.0).

§ Simplified Quadratic Reconstruction

Several strategies exist for piecewise quadratic reconstruction. As a general design criterion we require that the reconstruction exhibit quadratic precision (that the reconstruction be exact whenever the solution varies quadratically). This is sometimes called the property of k -exactness. Recall that a quadratic polynomial contains six degrees of freedom in two dimensions. This means that the support (stencil) of the reconstruction operator must contain at least six members. In refs. [16] and [17] this is accomplished by increasing the physical support on the mesh until six or more members are included. This approach has several pitfalls. Increasing the physical support may not always be possible due to the presence of boundaries. In this situation either the data support must be shifted in an unnatural way or the order of polynomial reconstruction must be lowered. Increasing the physical support also has the undesirable effect of bringing less relevant data into the reconstruction. One example would be data reconstruction in a flow field containing two shock waves in close proximity.

Another approach to higher order reconstruction is to add additional degrees of freedom into the solution representation. In our approach a quadratic element approximation is used, see Fig. 4.0. The solution unknowns are the six nodal values. These values uniquely describe a quadratic function within the element.

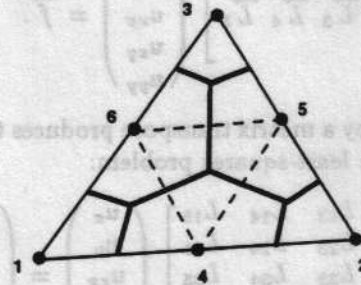


Figure 4.0 Six noded quadratic element with control volume tessellation (bold lines).

The control volumes for the finite-volume method are then formed from a tessellation of the elements. The particular tessellation which we prefer is obtained by connecting centroids and edges as shown in Fig. 4.0.

For each control volume surrounding a vertex or midside node, v_0 , a quadratic polynomial of the form

$$u(x, y)_0 = u_0 + \Delta \mathbf{r}^T \nabla u_0 + \frac{1}{2} \Delta \mathbf{r}^T H_0 \Delta \mathbf{r} \quad (5.0)$$

must be reconstructed from surrounding data. In this equation ∇u is the usual solution gradient and H is the Hessian matrix of second derivatives

$$H = \begin{bmatrix} u_{xx} & u_{xy} \\ u_{xy} & u_{yy} \end{bmatrix}$$

The basic solution procedure for the Euler and Navier-Stokes equations is identical to that described earlier, namely reconstruction, flux evaluation, and evolution. Once again the difficult task is data reconstruction given values of the solution at nodes of the mesh.

Least-Squares Quadratic Reconstruction

Following the procedure developed for linear reconstruction, we again consider two representations of the solution (continuous $u^{int}(x, y)$ and discontinuous $u^{recon}(x, y)$). We again seek to minimize the L_2 norm of the distance between these functions as sampled at flux quadrature points. This yields the following non-square matrix problem:

$$\begin{bmatrix} \Delta x_1 & \Delta y_1 & \frac{\Delta x_1^2}{2} & \Delta x_1 \Delta y_1 & \frac{\Delta y_1^2}{2} \\ \Delta x_2 & \Delta y_2 & \frac{\Delta x_2^2}{2} & \Delta x_2 \Delta y_2 & \frac{\Delta y_2^2}{2} \\ \Delta x_3 & \Delta y_3 & \frac{\Delta x_3^2}{2} & \Delta x_3 \Delta y_3 & \frac{\Delta y_3^2}{2} \\ \vdots & \vdots & \vdots & \vdots & \vdots \\ \Delta x_i & \Delta y_i & \frac{\Delta x_i^2}{2} & \Delta x_i \Delta y_i & \frac{\Delta y_i^2}{2} \\ \vdots & \vdots & \vdots & \vdots & \vdots \end{bmatrix} \begin{pmatrix} u_x \\ u_y \\ u_{xx} \\ u_{xy} \\ u_{yy} \end{pmatrix} = \begin{pmatrix} \Delta u_1 \\ \Delta u_2 \\ \Delta u_3 \\ \vdots \\ \Delta u_i \\ \vdots \end{pmatrix}$$

where $\Delta u = u^{int} - u_0$ for each quadrature point. The matrix equation can also be written symbolically as

$$\begin{bmatrix} \vec{L}_1 & \vec{L}_2 & \vec{L}_3 & \vec{L}_4 & \vec{L}_5 \end{bmatrix} \begin{pmatrix} u_x \\ u_y \\ u_{xx} \\ u_{xy} \\ u_{yy} \end{pmatrix} = \vec{f}. \quad (6.0)$$

Multiplication by a matrix transpose produces the normal form of the least-squares problem:

$$\begin{bmatrix} L_{11} & L_{12} & L_{13} & L_{14} & L_{15} \\ L_{12} & L_{22} & L_{23} & L_{24} & L_{25} \\ L_{13} & L_{23} & L_{33} & L_{34} & L_{35} \\ L_{14} & L_{24} & L_{34} & L_{44} & L_{45} \\ L_{15} & L_{25} & L_{35} & L_{45} & L_{55} \end{bmatrix} \begin{pmatrix} u_x \\ u_y \\ u_{xx} \\ u_{xy} \\ u_{yy} \end{pmatrix} = \begin{pmatrix} f_1 \\ f_2 \\ f_3 \\ f_4 \\ f_5 \end{pmatrix} \quad (7.0)$$

This equation requires the calculation of 15 inner products L_{ij} and 5 inner products f_i . Note that certain identities exist relating L_{ij} which further reduce the number of L_{ij} needed to 12.

Two concerns arise in the general implementation of this least-squares technique. First, we desire that the reconstruction be invariant to affine coordinate transformations, i.e. translation, rotation, dilatation, and shear. These effects can be eliminated or reduced by a preimage mapping to a normalized control volume, see for example [16]. Second, the least-squares solution by way of normal equations can be poorly conditioned. Numerical evidence indicates that for highly stretched meshes (aspect ratio > 100000) and linear reconstruction, the method does not suffer from conditioning problems using 64 bit arithmetic. However, when implementing quadratic reconstruction, we have noted some conditioning problems when the cell aspect ratio gets very large. Other methods for solving the basic least-squares problem are much less sensitive to the matrix condition number: Householder transforms, SVD, etc. For highly stretched meshes the use of these methods may be a necessity. This is an area of current research.

§ Enforcing Monotonicity of the Reconstruction

Consider the reconstructed quadratic polynomial for the control volume surrounding v_0

$$u(x, y)_0 = u_0 + \Delta \mathbf{r}^T \nabla u_0 + \frac{1}{2} \Delta \mathbf{r}^T H_0 \Delta \mathbf{r}.$$

One approach to enforcing monotonicity of the reconstruction is to introduce a parameter Φ into the reconstruction polynomial

$$u(x, y)_0 = u_0 + \Phi_0 \left[\Delta \mathbf{r}^T \nabla u_0 + \frac{1}{2} \Delta \mathbf{r}^T H_0 \Delta \mathbf{r} \right] \quad (8.0)$$

with the goal of finding the largest admissible $\Phi_0 \in [0, 1]$ while invoking a monotonicity principle that values of the reconstructed function must not exceed the maximum and minimum of neighboring nodal values and u_0 . To calculate Φ_0 first compute

$$u_0^{min} = \min(u_0, u_{neighbors}), \quad u_0^{max} = \max(u_0, u_{neighbors})$$

then require that $u_0^{min} \leq u(x, y)_0 \leq u_0^{max}$. Extrema in $u(x, y)_0$ can occur anywhere in the interior or on the boundary of the control volume surrounding v_0 . Determining the location and type of extrema is clumsy and computationally expensive. One approximation which considerably simplifies the task is to interrogate the reconstructed polynomial for extreme values at the

quadrature points used in the flux integration. For each quadrature point on the boundary of the control volume, evaluate the reconstructed polynomial u_i to determine the limiting value of Φ_0 , which satisfies:

$$\Phi_0 = \begin{cases} \min \left(1, \frac{u_0^{\max} - u_0}{u_i - u_0} \right), & \text{if } u_i - u_0 > 0 \\ \min \left(1, \frac{u_0^{\min} - u_0}{u_i - u_0} \right), & \text{if } u_i - u_0 < 0 \\ 1 & \text{if } u_i - u_0 = 0 \end{cases}$$

This limiting procedure is very effective in removing spurious solution oscillations although the discontinuous nature of the limiter can hinder steady-state convergence of the scheme.

§ Numerical Results

A variety of fluid flows have been computed using the reconstruction schemes described earlier. For purpose of comparison, computations have also been performed using other state-of-the-art methods: the fluctuation splitting method of Roe [1] and Deconinck *et al.* [2] as well as a variant of the Galerkin least-square finite-element method developed by Hansbo [3] and Hansbo and Johnson [4]. These methods are described in appendices A and B. Both of these methods have been reformulated in terms of "edge formulas" which makes them easily retrofitted into existing computer codes which use edge data structures. Table 1.0 summarizes the various schemes, their data support in graph distance, and the relative CPU time for explicit evaluation of the steady-state discretization. These estimates are based on a fully vectorized computer implementation.

Scheme	Support	Cpu Units
Piecewise constant reconstruction	1	1
Piecewise linear reconstruction	2	3
Fluctuation splitting	1	11
Galerkin least-squares	1	10
Piecewise quadratic reconstruction	2	22

Table 1.0 Comparison of data support and cpu times for various schemes.

In the remainder of this section numerical results are presented comparing the various schemes. Five test problems are used in the numerical comparisons: scalar circular advection, supersonic and transonic Euler flow, laminar boundary-layer flow, and general compressible Navier-Stokes flow.

Scalar Circular Advection

The first test problem solves the two-dimensional scalar advection equation

$$u_t + (yu)_x - (xu)_y = 0$$

or equivalently

$$u_t + \vec{\lambda} \cdot \nabla u = 0, \quad \vec{\lambda} = (y, -x)^T$$

on a grid centered about the origin, see Fig. 5.0. Discontinuous inflow data is specified along an interior cut line, $u(x, 0) = 1$ for $-0.6 < x < -0.3$ and $u(x, 0) = 0$, otherwise. The exact solution is a solid body rotation of the cut line data throughout the domain.

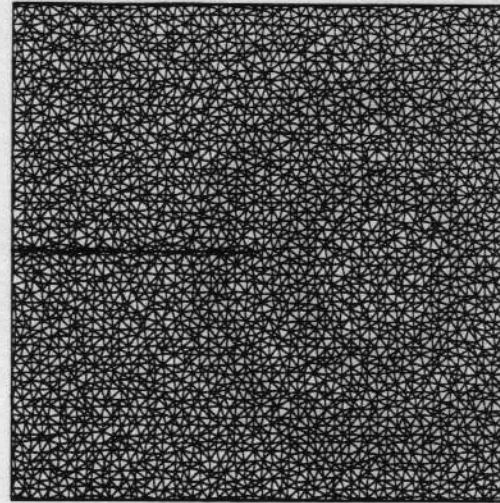


Figure 5.0 Grid for the circular advection problem.

The discontinuities admitted by this equation are similar to the linear contact and slip line solutions admitted by the Euler equations. Linear discontinuities are often more difficult to compute accurately than nonlinear shock wave solutions which naturally steepen due to converging characteristics. Figures 5.1-5.5 display solution contours for the various schemes.

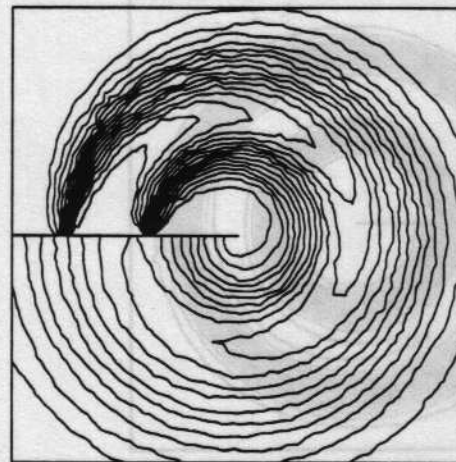


Figure 5.1 Solution contours, piecewise constant reconstruction.

The piecewise constant reconstruction scheme excessively smears the discontinuities. The remaining methods all perform very well. The piecewise linear reconstruction, fluctuation splitting, and Galerkin least-squares schemes all produce similar results with similar spreading of the discontinuities. Note that some variation in results can be obtained with the Galerkin least-squares solution with discontinuity capturing operator depending on the choice of element length scale (cell diameter, incircle, circumcircle, etc.).

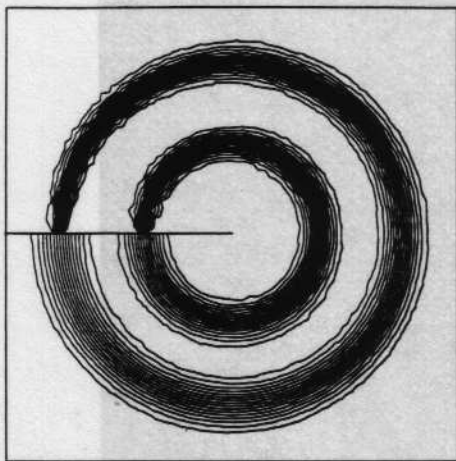


Figure 5.2 Solution contours, piecewise linear reconstruction.

The results for the piecewise quadratic reconstruction are shown in Fig. 5.5. The width of the discontinuities is substantially reduced with very little observable grid dependence.

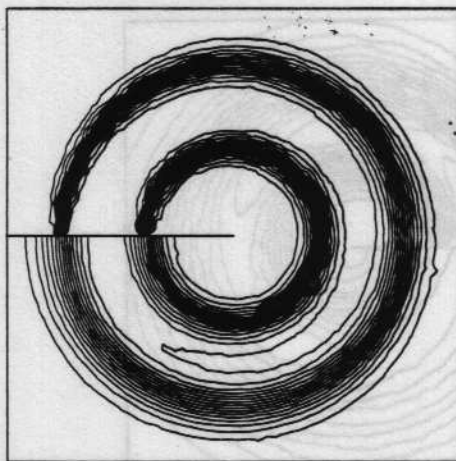


Figure 5.3 Solution contours, fluctuation splitting scheme.

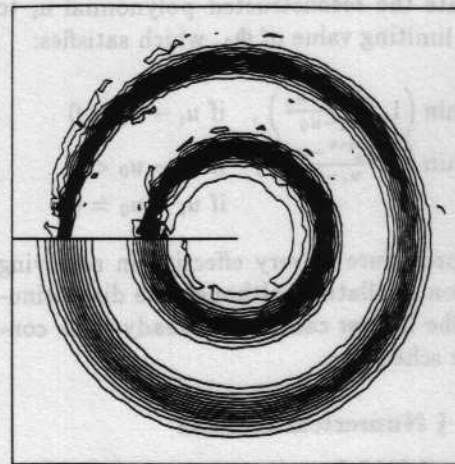


Figure 5.4 Solution contours, Galerkin Least-Squares.

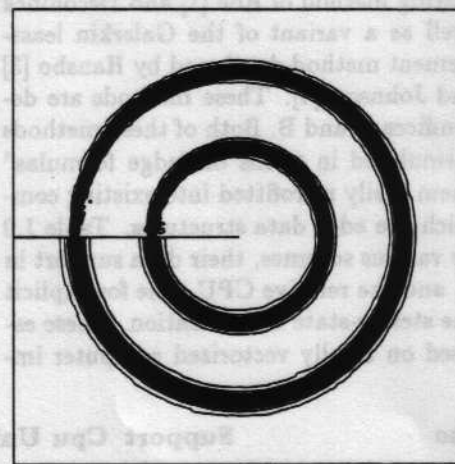


Figure 5.5 Solution contours, piecewise quadratic reconstruction.

Supersonic Oblique Shock Reflections

Two supersonic streams ($M=2.50$ and $M=2.31$) are introduced at the left boundary. These streams interact producing a pattern of supersonic shock reflections down the length of the converging channel, see Fig. 6.0. The grid is a subdivided 15×52 mesh with perturbed coordinates.

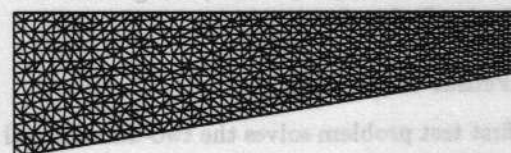


Figure 6.0 Channel Grid.

Solution Mach contours are shown in Figs. 6.1-6.5. Figure 6.6 graphs density profiles along a horizontal cut at 70 percent the vertical height of the left boundary. As expected, the piecewise constant reconstruction scheme severely smears the shock system while the schemes based on a linear solution variation, Figs. 6.2-6.4, all perform surprisingly well. The piecewise quadratic approximation, Fig. 6.5, shows some improvement in shock wave width although the improvement is probably due to the increased number of unknowns in the quadratic element.



Figure 6.1 Mach contours, piecewise constant reconstruction.



Figure 6.2 Mach contours, piecewise linear reconstruction.



Figure 6.3 Mach contours, fluctuation splitting.

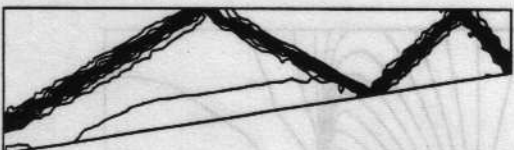


Figure 6.4 Mach contours, Galerkin least-squares.



Figure 6.5 Mach contours, piecewise quadratic reconstruction.

This is not a surprising result since the solution has

large regions of constant flow which do not benefit greatly from the quadratic approximation. At solution discontinuities the quadratic scheme reduces to a low order approximation which again negates the benefit of the quadratic reconstruction.

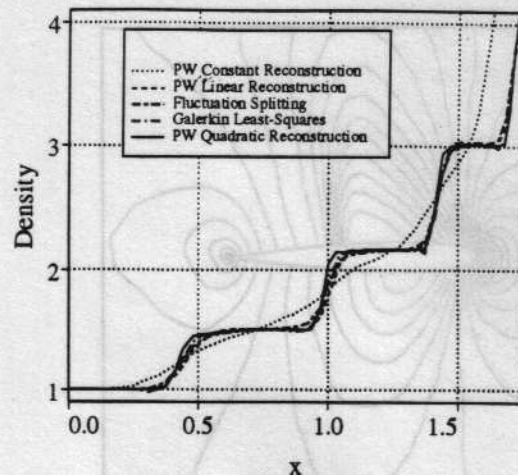


Figure 6.6 Density profile, $y/h = .70$.

Transonic Airfoil Flow

The next calculation consists of transonic Euler flow about a NACA 0012 airfoil at $M = .80$ and $\alpha = 1.25^\circ$. The solution consists of an upper and lower surface shock wave and a trailing edge slip line. The grid used for all calculations is shown in Fig. 7.0.

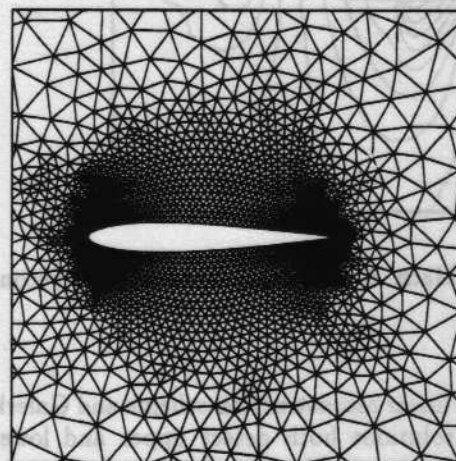


Figure 7.0 Closeup of grid about NACA 0012 airfoil.

Solution Mach contours are shown in Figs. 7.1-7.5 for the various schemes. The surface pressure coefficient distributions are plotted in Fig. 7.6. The solution obtained using piecewise constant reconstruction misses the lower surface shock wave and trailing edge slip line.

The fluctuation splitting method also misses these features but computes a stronger (more accurate) upper surface shock. The preshock oscillations are apparently attributable to the choice of wave model and have been observed elsewhere, see Powell *et al.* [23].

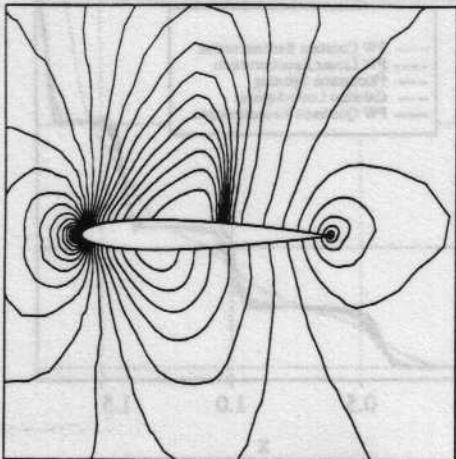


Figure 7.1 Mach contours, piecewise constant reconstruction.

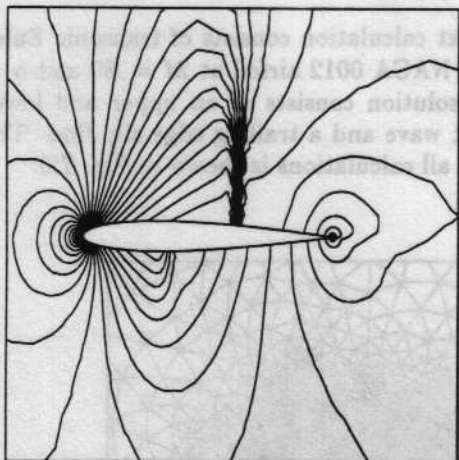


Figure 7.2 Mach contours, piecewise linear reconstruction.

The piecewise linear reconstruction scheme and Galerkin least-squares solutions both detect upper and lower surface shock waves as well as the slip line. Once again note that the amount of discontinuity capturing operator added to the Galerkin least-squares scheme has been approximately optimized and improved results might be obtainable. As expected the numerical solution obtained with piecewise quadratic reconstruction is superior to the other methods. Both the upper and lower surface shocks are crisply captured.

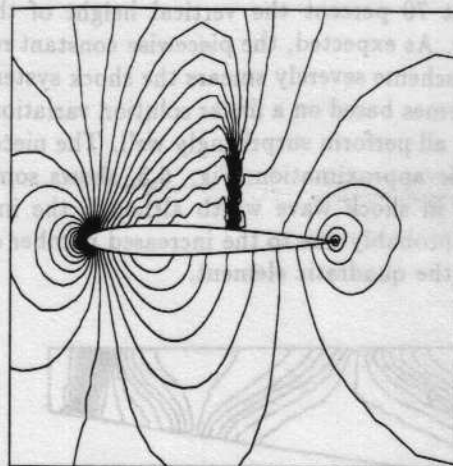


Figure 7.3 Mach contours, fluctuation splitting with Roe six-wave model.

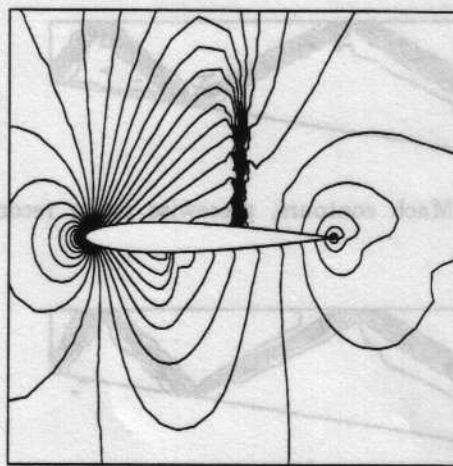


Figure 7.4 Mach contours, Galerkin Least-Squares.

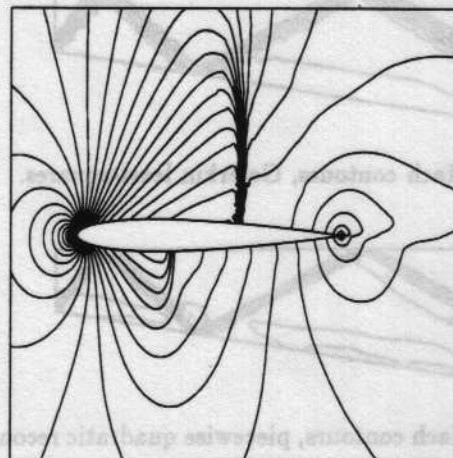


Figure 7.5 Mach contours, piecewise quadratic recon-

struction.

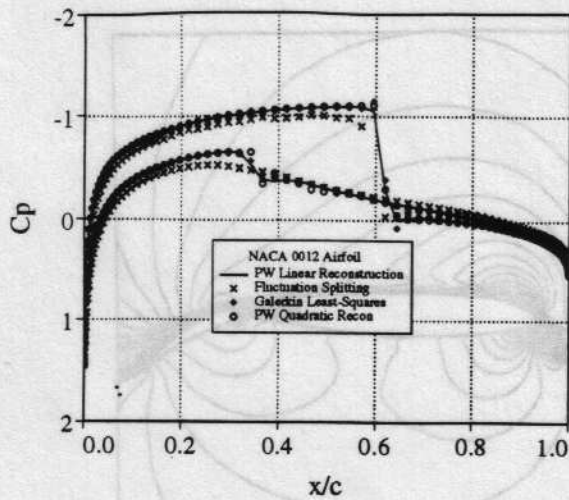


Figure 7.6 C_p distributions on NACA 0012 airfoil surface.

Blasius Boundary-Layer

A self-similar laminar boundary-layer is simulated on a 10×20 subdivided quadrilateral mesh, see Fig. 8.0. An analytical Blasius profile is specified at inflow and computations at low Mach number ($M = .08$) were performed using the reconstruction schemes.

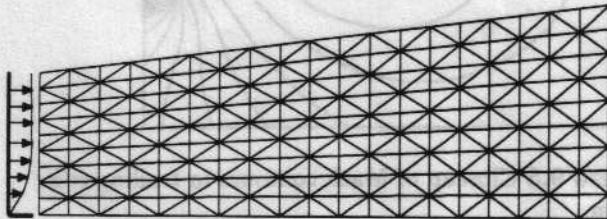


Figure 8.0 Coarse Flat Plate Grid.

Viscous terms have been discretized in finite-volume form using the continuous triangle interpolants (linear or quadratic) and integration quadrature rules consistent with these interpolants. For the piecewise constant and linear schemes this produces the viscous term weights described in appendix A and in Barth [15]. Figure 8.1 graphs the velocity profile which has been vertically sampled at $x/L = .88$. Data is plotted at locations corresponding to the intersection of this vertical line and the edges of the mesh. This results in a somewhat irregular spacing of data points.

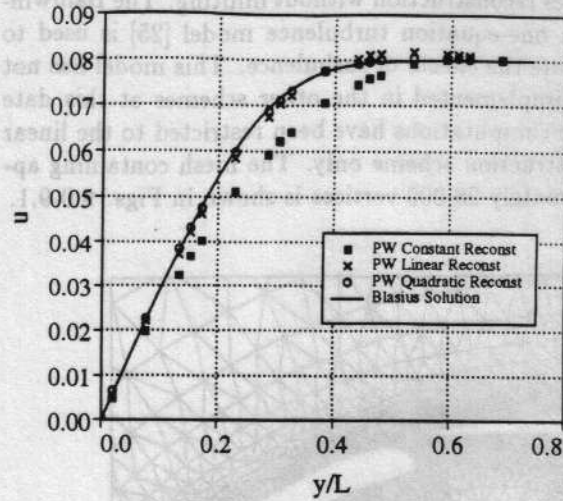


Figure 8.1 Velocity profiles at $x/L = .88$.

The piecewise constant reconstruction performs rather poorly owing to the excessive diffusion in the Euler scheme. The linear reconstruction scheme (without limiting) produces a reasonably accurate solution with a slight overshoot in the outer edge of the boundary-layer. The quadratic scheme performs very well with a slight error in the region of maximum curvature. Both higher order methods appear to have acceptable accuracy for this problem.

Multi-Element Airfoil Flow

Turbulent high Reynolds number flow ($M = .2$, $\alpha = 8.2^\circ$, $Re = 9$ million) is computed about a 3-element airfoil configuration. Experimental data is available at these conditions, see Valarezo *et al.* [24].

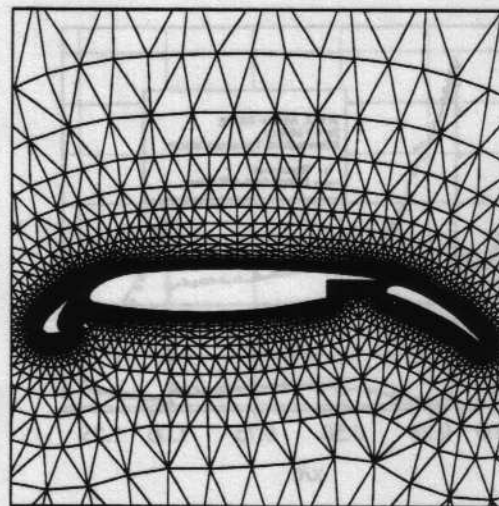


Figure 9.0 Grid about multi-element airfoil configuration.

Computations were performed using the linear least-squares reconstruction without limiting. The Baldwin-Barth one-equation turbulence model [25] is used to simulate the effects of turbulence. This model has not been implemented in the other schemes at this date so the computations have been restricted to the linear reconstruction scheme only. The mesh containing approximately 28,000 vertices is shown in Figs. 9.0-9.1.

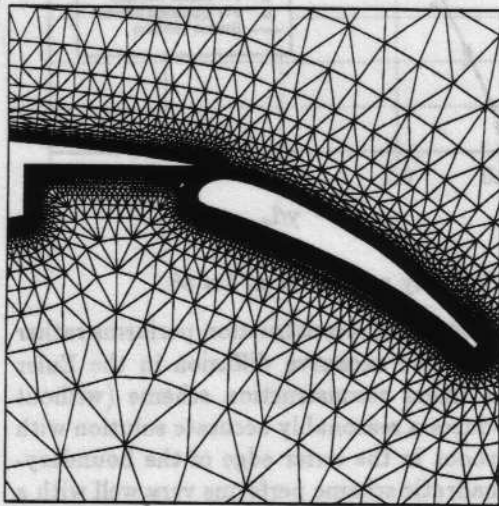


Figure 9.1 Closeup of grid near flap region.

The pressure coefficient distribution is graphed in Fig. 9.3 for the computation and experiment. The agreement with experiment is reasonably good although the mesh resolution is inadequate in the wake regions of the flow. This can be seen in the Mach contour plots shown in figures 9.4-9.5. Proper mesh resolution of the wake flow is an excellent opportunity for mesh adaptation although we have not developed an adaptation procedure for this purpose.

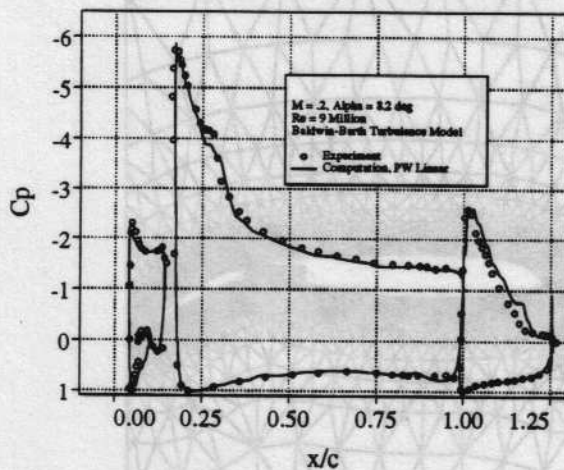


Figure 9.3 C_p distribution on multi-element airfoil surface.

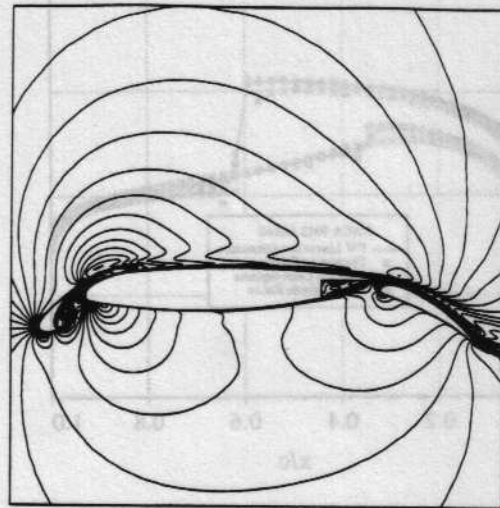


Figure 9.4 Mach contours about multi-element airfoil.

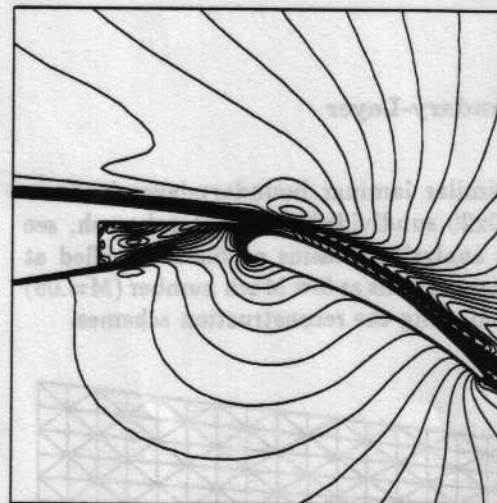


Figure 9.5 Closeup of Mach contours in trailing edge region.

§Conclusions

The numerical results indicate that the higher order accurate reconstruction methods (piecewise linear and piecewise quadratic) offer a substantial improvement over the basic low order (piecewise constant) scheme. The linear reconstruction scheme appear to have the same basic level of accuracy as the Galerkin least-squares finite-element scheme and the fluctuation splitting scheme. The finite-volume scheme with quadratic reconstruction is a noticeable improvement over the lower order reconstruction methods but the computational cost is relatively high. Issues still remain concerning the conditioning of reconstruction methods for highly stretched triangulations.

§ Appendix A: Review of the Fluctuation Splitting Approach of Roe [1] and Deconinck et al [2]

In the following paragraphs we review the fluctuation splitting approach of Roe [1] and Deconinck *et al.* [2] for scalar advection equations. An edge formulation of the fluctuation splitting scheme is derived which makes the scheme easily implemented into computer codes using an edge data structure. Next, we show the extension of fluctuation splitting to scalar advection-diffusion equations and a hybrid fluctuation splitting scheme which improves upon the basic fluctuation splitting scheme without sacrificing positivity (monotonicity) of the scheme. Finally, the extension of the fluctuation splitting method to the Euler equations using the Roe six wave model [2] will be briefly reviewed.

N-scheme For Scalar Advection Equations

Consider discretizations of the integral scalar conservation law equation

$$\frac{\partial}{\partial t} \int_{\Omega} u \, da + \int_{\Omega} \nabla \cdot \vec{F} \, da = 0, \quad \vec{F} = f\hat{i} + g\hat{j} \quad (A.1)$$

on simplicial meshes (triangulations) with solution unknowns given at vertices of the mesh. Next define the fluctuation in a triangle T , Φ_T ,

$$\Phi_T = - \int_T \nabla \cdot \vec{F} \, da$$

or

$$\Phi_T = -A_T \bar{\lambda}_T \cdot \nabla u \quad (A.2)$$

where $\bar{\lambda}_T$ is constructed via mean-value linearization such that an equality exists. The primary idea in fluctuation splitting is to distribute the fluctuation Φ back to the three vertices (see Fig. A.1) in a characteristically correct way.

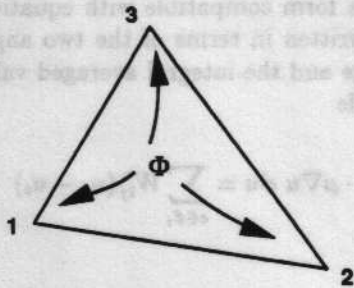


Figure (A.1) Distribution of fluctuation among vertices.

At a given vertex, v_i , the update scheme can be written in the following form for all triangles incident to v_i .

$$u_i^{n+1} = u_i^n + \frac{\Delta t}{A_i} \sum_{T \in \tau_i} \beta_T^{v_i} \Phi_T \quad (A.3)$$

Discrete conservation dictates that for a triangle T with vertices v_1, v_2, v_3 a fundamental constraint that

$$\beta_T^{v_1} + \beta_T^{v_2} + \beta_T^{v_3} = 1. \quad (A.4)$$

Recall that if $\beta_T^i = \frac{1}{3}$ and $A_i = \sum_T A_T/3$ then a Galerkin-like discretization akin to central differencing results. In the work by Roe [1] and Deconinck *et al.* [2] upwind discretizations taking the following form

$$u_i^{n+1} = u_i^n + \frac{\Delta t}{A_i} \sum_{T \in \tau_i} \gamma_T^{v_i} \quad (A.5)$$

are derived where

$$\beta_T^{v_i} = \frac{\gamma_T^{v_i}}{\Phi_T} \quad \text{with} \quad \Phi_T = \gamma_T^{v_1} + \gamma_T^{v_2} + \gamma_T^{v_3}.$$

In particular, they consider a distribution scheme (the N-Scheme) which is monotonicity preserving with γ dependent on $\bar{\lambda}$. The scheme can be written in the following form:

$$u_i^{n+1} = u_i^n + \sum_j w_{ij} (u_j - u_i) \quad \text{with} \quad w_{ij} \geq 0. \quad (A.6)$$

This equation and inequality embodies a maximum principle. At steady-state, the solution at v_i is a positive weighted average adjacent neighbors. Depending on the advection direction $\bar{\lambda}$ the scheme *downwind* distributes the fluctuation as depicted in Fig. (A.2), details of the derivation can be found in [1].

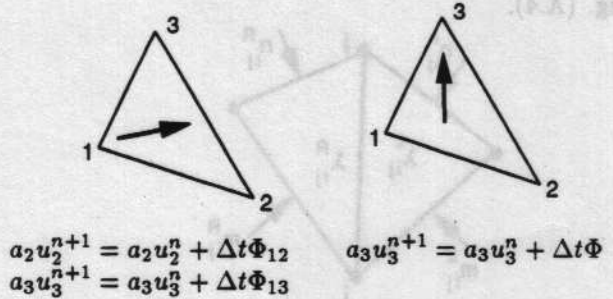


Figure (A.2) Schematic of N-scheme.

Deconinck gives the following succinct formula for $\gamma_T^{v_i}$ in the N-Scheme

$$\gamma_T^{v_i} = \frac{(k_i)^+}{2 \sum_{j=1}^3 (k_j)^+} \sum_{j=1}^3 (k_j)^- (u_i^n - u_j^n), \quad i = 1, 2, 3 \quad (A.7)$$

where $k_j = \vec{\lambda}_T \cdot \mathbf{n}_j$ and \mathbf{n}_j is the scaled normal vector for the edge opposite local vertex j as shown in Fig. (A.3).

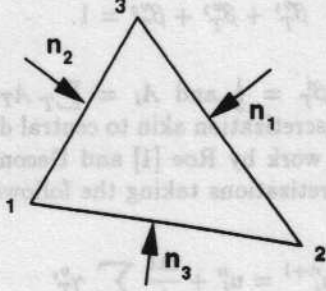


Figure (A.3) Triangle T with local indexing.

The update scheme becomes

$$u_i^{n+1} = u_i^n + \frac{\Delta t}{A_i} \sum_{T \in \mathcal{T}_i} \frac{(k_i)^+}{2\sigma_T} \sum_{j=1}^3 (k_j)^- (u_{v_i}^n - u_{v_j}^n) \quad (\text{A.8})$$

for $i = 1, 2, 3$ and $\sigma_T = \sum_{j=1}^3 (k_j)^+$. This formula can be manipulated into the following *edge* formula for all edges $e(v_i, v_j)$ incident to v_i

$$u_i^{n+1} = u_i^n + \frac{\Delta t}{A_i} \sum_{e \in \mathcal{E}_i} W_{ij} (u_j - u_i) \quad (\text{A.9})$$

where

$$W_{ij} = - \left[\frac{(\vec{\lambda}_{ij}^L \cdot \mathbf{n}_{ij}^L)^+ (\vec{\lambda}_{ij}^L \cdot \mathbf{m}_{ij}^L)^-}{2\sigma_{ij}^L} + \frac{(\vec{\lambda}_{ij}^R \cdot \mathbf{n}_{ij}^R)^+ (\vec{\lambda}_{ij}^R \cdot \mathbf{m}_{ij}^R)^-}{2\sigma_{ij}^R} \right] \quad (\text{A.10})$$

and the scaled normal vectors \mathbf{n} and \mathbf{m} are depicted in Fig. (A.4).

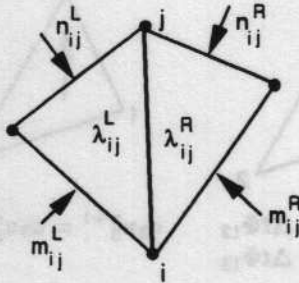


Figure (A.4) Local configuration for edge $e(v_i, v_j)$.

Although the N-scheme is monotone, the scheme allows a triangle in equilibrium $\vec{\lambda} \cdot \nabla u = 0$ with nonzero gradient to send nonzero contributions with zero sum to downstream vertices. This degrades the accuracy of steady-state solutions since the scheme is not linearity preserving and only exactly preserves constant solutions.

NN-scheme For Scalar Advection Equations

By introducing an additional level on nonlinearity, the equilibrium deficiency of the N-scheme can be overcome. Define the frontal advection vector as the projection of the advection vector onto the cell gradient vector

$$\vec{\lambda}^m = \frac{\vec{\lambda} \cdot \nabla u}{\nabla u \cdot \nabla u} \nabla u \quad (\text{A.11})$$

Note that the use of a frontal advection vector leaves the fluctuation unchanged

$$\Phi_T = -A_T \vec{\lambda} \cdot \nabla u = -A_T \vec{\lambda}^m \cdot \nabla u$$

The use of the frontal advection vector *does* change the distribution formulas and insures that cells in equilibrium send no contributions to downstream vertices. This added nonlinearity is not always needed. In the single target distribution configuration shown in Fig. (A.2), the scheme is both positive and linearity preserving. Therefore the frontal advection speeds need only be used in the NN-scheme whenever the N-scheme predicts a multiple target distribution. This enhancement greatly improves the robustness of the NN-scheme.

Hybrid NN-scheme For Scalar Advection-Diffusion Equations

Consider equation (A.1) with diffusion term added

$$\frac{\partial}{\partial t} \int_{\Omega} u \, da + \int_{\Omega} \nabla \cdot \vec{F} \, da = \int_{\Omega} \nabla \cdot \mu \nabla u \, da \quad (\text{A.12})$$

In Barth [15] we considered the standard finite-volume and Galerkin finite-element discretization for the right-hand-side of equation (A.12). The discretization can be written in a form compatible with equation (A.9) with weights written in terms of the two angles subtending an edge and the integral averaged values of μ for each triangle

$$\int_{\Omega} \nabla \cdot \mu \nabla u \, da = \sum_{e \in \mathcal{E}_i} W_{ij}^v (u_j - u_i)$$

with

$$W_{ij}^v = \frac{1}{2} [\bar{\mu}_{ij}^L \cotan(\alpha_{ij}^L) + \bar{\mu}_{ij}^R \cotan(\alpha_{ij}^R)] \quad (\text{A.13})$$

or equivalently using edge normals

$$W_{ij}^v = -\frac{1}{2} \left[\bar{\mu}_{ij}^L \frac{(\mathbf{n}_{ij}^L \cdot \mathbf{m}_{ij}^L)}{|\mathbf{n}_{ij}^L \times \mathbf{m}_{ij}^L|} + \bar{\mu}_{ij}^R \frac{(\mathbf{n}_{ij}^R \cdot \mathbf{m}_{ij}^R)}{|\mathbf{n}_{ij}^R \times \mathbf{m}_{ij}^R|} \right] \quad (\text{A.14})$$

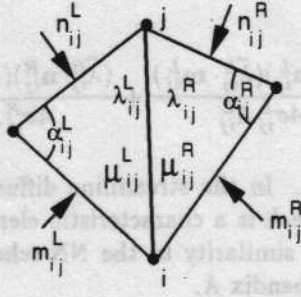


Figure (A.5) Local configuration for edge $e(v_i, v_j)$.

It is well known that a sufficient condition for positivity of weights is that all angles in the triangulation are acute. This is easily seen from equation (A.13). The generalization to n -dimensional triangulations is that all simplices are self-centered (the circumcenter is contained within the simplex). Sharper bounds can sometimes be obtained from (A.13). For example in two dimensions with μ constant it is known that for general point distributions and boundary data that a necessary and sufficient condition for positivity (and a discrete maximum principle) is that the triangulation be a Delaunay triangulation. This result is directly obtained from (A.13). Recall that valid Delaunay triangulations can have obtuse angles approaching 180° .

In diffusion dominated portions of the flow it is no longer necessary to impose the positivity conditions on the weights as given (A.10). It is possible to have negative weights appearing in the advection operator such that when combined with the weights appearing in the diffusion operator the overall scheme is positive. A natural choice of advection schemes in the diffusion dominated limit is obtained with $\beta_T^v = 1/3$ since the Galerkin-like advection scheme is the best approximation to the true solution in an energy norm. An obvious strategy is to introduce a new parameter $\theta \in [0, 1]$ such that

$$\begin{aligned}\theta = 0 & \quad \text{diffusion dominated} \\ \theta = 1 & \quad \text{advection dominated}\end{aligned}$$

where the actual value of θ is determined from positivity considerations for the entire advection-diffusion discretization. The Galerkin-like advection scheme can be written in a form similar to (A.8)

$$u_i^{n+1} = u_i^n + \frac{\Delta t}{A_i} \sum_{T \in \mathcal{T}_i} \frac{1}{6} \sum_{j=1}^3 (k_j)(u_{v_i}^n - u_{v_j}^n) \quad (\text{A.15})$$

for $i = 1, 2, 3$. The entire advection update scheme

with variable parameter θ would take the form

$$u_i^{n+1} = u_i^n + \frac{\Delta t}{A_i} \sum_{T \in \mathcal{T}_i} \left[\theta_T \frac{(k_i)^+}{2\sigma_T} \sum_{j=1}^3 (k_j)^- (u_{v_i}^n - u_{v_j}^n) + (1 - \theta_T) \sum_{j=1}^3 \frac{k_j}{6} (u_{v_i}^n - u_{v_j}^n) \right]$$

or in terms of edge weights

$$W_{ij} = \left[-\theta_{ij}^L \frac{(\vec{\lambda}_{ij}^L \cdot \vec{n}_{ij}^L)^+ (\vec{\lambda}_{ij}^L \cdot \vec{m}_{ij}^L)^-}{2\sigma_{ij}^L} + (1 - \theta_{ij}^L) \frac{(\vec{\lambda}_{ij}^L \cdot \vec{m}_{ij}^L)}{6} \right] + \left[-\theta_{ij}^R \frac{(\vec{\lambda}_{ij}^R \cdot \vec{n}_{ij}^R)^+ (\vec{\lambda}_{ij}^R \cdot \vec{m}_{ij}^R)^-}{2\sigma_{ij}^R} + (1 - \theta_{ij}^R) \frac{(\vec{\lambda}_{ij}^R \cdot \vec{m}_{ij}^R)}{6} \right] \quad (\text{A.16})$$

When combined with the diffusion term weights (A.14), the task is to find the largest θ in each triangle T such that

$$\theta \frac{(\vec{\lambda} \cdot \vec{n})^+ (\vec{\lambda} \cdot \vec{m})^-}{2\sigma} + (1 - \theta) \frac{(\vec{\lambda} \cdot \vec{m})}{6} + \frac{\mu (\vec{n} \cdot \vec{m})}{2 |\vec{n} \times \vec{m}|} \leq 0$$

for all possible combinations of \vec{m} and \vec{n} in T . For self-centered meshes, a solution is readily obtained with $\theta \in [0, 1]$. We find that this hybrid strategy for scalar advection-diffusion equations is very useful for solving the one-equation turbulence model given in [25].

Extension to the Euler Equations

The basic notion is to decompose the fluctuation into a finite number of eigensolutions of the two-dimensional Euler equations:

$$\Phi = \sum_m \alpha_m \lambda_m \mathbf{r}_m$$

where α is the wave strength, λ the wave speed, and \mathbf{r} a right eigenvector of the two-dimensional Euler equations. These quantities are a function of the individual wave orientations. The unknown wave orientations, speeds, and strengths are determined from the fluid state and gradient. A detailed discussion of this decomposition is beyond the scope of this paper, see [1, 2, 23]. For the Roe model used in the present computations, six eigensolutions corresponding to four acoustic waves, one entropy wave, and one shear wave are used in the decomposition. Once the decomposition is known, the scalar advection scheme can be applied on a wave by wave basis.

§ Appendix B: Review of the Galerkin Least-Squares Approach of Hansbo [3] and Hansbo and Johnson [4]

In this section we review the Galerkin least-squares finite-element method with nonlinear discontinuity capturing operator. The formulation given here assumes

uniformly shaped elements. For a discussion of formulations suitable for computation on stretched elements see Shakib [14]. We begin by reviewing the least-squares finite-element operator with linear elements. An edge formulation of the least-squares operator is presented which makes the scheme easily implemented in computer codes using an edge data structure. We then review the conservative variable approach of Hansbo [3] and Hansbo and Johnson [4]. Finally, we review the discontinuity capturing operator given in [3] for both scalar and systems of equations.

Galerkin formulation

Consider the linear advection equation

$$u_t + \tilde{\lambda} \cdot \nabla u = 0. \quad (B.1)$$

Multiplying by the trial functions w followed by integration over the domain produces a weak form of (B.1)

$$\frac{\partial}{\partial t} \int_{\Omega} w u \, da + \int_{\Omega} w (\tilde{\lambda} \cdot \nabla u) \, da = 0. \quad (B.2)$$

When the trial and solution function spaces are identical, a Galerkin discretization is obtained. In the present case w and u are linear in space and piecewise constant in time. Note that the resulting mass-lumped update scheme would be identical to (A.15). For the linear differential equation the scheme is isoenergetic (neutrally stable) and when nonlinearity is introduced into (B.1) additional measures must be taken to insure stability. One technique for stabilizing the basic Galerkin scheme is the addition of symmetric bilinear (quadratic) terms to equation (B.2). The following section describes two possibilities.

Least-Squares Stabilization

Consider stabilization of the basic Galerkin method by the addition of the bilinear least-squares term to the right-hand-side of (B.2).

$$B(u, w)_{LS} = - \int_{\Omega} (u_t + \tilde{\lambda} \cdot \nabla u) \tau (w_t + \tilde{\lambda} \cdot \nabla w) \, da \quad (B.3)$$

To understand the energy consequences of this term simply replace w by u . For $\tau > 0$ we have that $B(u, u)_{LS} < 0$ which implies that this term would remove energy from the basic Galerkin system. For steady-state computations we need only consider (B.3) with time terms removed.

$$B(u, w)_{LS} = - \int_{\Omega} (\tilde{\lambda} \cdot \nabla u) \tau (\tilde{\lambda} \cdot \nabla w) \, da \quad (B.4)$$

Discretization of this term with linear space elements u and w yields an edge formula

$$\int_{\Omega} (\tilde{\lambda} \cdot \nabla u) \tau (\tilde{\lambda} \cdot \nabla w) \, da = \sum_{e \in \mathcal{E}_i} W_{ij} (u_j - u_i)$$

with

$$W_{ij} = \left[\frac{(\tilde{\lambda}_{ij}^L \cdot \mathbf{n}_{ij}^L)(\tilde{\lambda}_{ij}^L \cdot \mathbf{m}_{ij}^L)}{4\sigma_{ij}^L A_{ij}^L} + \frac{(\tilde{\lambda}_{ij}^R \cdot \mathbf{n}_{ij}^R)(\tilde{\lambda}_{ij}^R \cdot \mathbf{m}_{ij}^R)}{4\sigma_{ij}^R A_{ij}^R} \right] \quad (B.5)$$

where $\sigma = 1/\tau$. In the streamline diffusion method $\sigma = |\lambda|/h$ where h is a characteristic element dimension. Note the similarity to the NN-scheme weights described in appendix A.

In the system case,

$$\mathbf{u}_t + A\mathbf{u}_x + B\mathbf{u}_y = 0 \quad (B.6)$$

the least-squares term takes the following form

$$- \int_{\Omega} (A\mathbf{u}_x + B\mathbf{u}_y)^T \tau (A\mathbf{w}_x + B\mathbf{w}_y) \, da \quad (B.7)$$

where τ is a matrix. The exact form of τ is a subject for debate. In the present implementation, we consider a formulation by Hansbro and Johnson [3] which solves the Euler equations in conserved variable form with τ given by

$$\tau = h(A^2 + B^2)^{-1/2}. \quad (B.8)$$

Numerical results with the basic Galerkin least-squares method indicate that further measures must be taken to prevent solution oscillations near discontinuities. These oscillations can be removed by the addition of the discontinuity capturing operator described in the next section.

Discontinuity Capturing Operator

Consider another symmetric bilinear term for stabilizing the Galerkin scheme

$$B(u, w)_{DC} = -h \int_{\Omega} \kappa (\nabla w \cdot \nabla u) \, da. \quad (B.9)$$

This term is a weak form of the viscous-like term

$$B(u, w)_{DC} = h \int_{\Omega} w \nabla \cdot \kappa \nabla u \, da. \quad (B.10)$$

Again we have that $B(u, u)_{DC} \leq 0$ if $\kappa \geq 0$. To prevent this term from destroying the accuracy of the scheme, κ is chosen in the following form:

$$\kappa = \frac{|\tilde{\lambda} \cdot \nabla u|}{|\nabla u| + \epsilon} \quad (B.11)$$

for small ϵ . This choice of κ vanishes when $\tilde{\lambda} \cdot \nabla u$ is small. This term is expected to be small when the solution is smooth and the element residuals are small. The simplest extension to systems replaces the absolute value by a vector norm. Although seemingly simplistic, this approximation works surprisingly well.

§ References

1. Roe, P.L., "Linear Advection Schemes on Triangular Meshes," Cranfield Inst., Report No. 8720, November, 1987.
2. Deconinck, H., Strujs, R., Bourgois, G., Paillère, H., Roe, P.L., "Multidimensional Upwind Methods for Unstructured Grids," AGARD Report R-787, ISBN 92-835-0671-5, May 1992.
3. Hansbo, P., "Explicit Streamline Diffusion Finite Element Methods for the Compressible Euler Equations in Conservation Variables," Report No. 1991-31, Department of Mathematics, Chalmers Inst. of Tech., Sweden, 1991.
4. Hansbo, P., and Johnson C., "Adaptive Streamline Diffusion Methods for Compressible Flow," Comput. Meth. Appl. Mech. Engrg., Vol. 87, 1991., pp. 267-280.
5. Slack, D. C., Walters, R. W., and Löhner, R., "An Interactive Adaptive Remeshing Algorithm for the Two-Dimensional Euler Equations", AIAA-90-0331, Jan. 8-11, 1990.
6. Whitaker, D. L., Slack, D. C., and Walters, R. W., "Solution Algorithms for the Two-Dimensional Euler Equations on Unstructured Meshes", AIAA-90-0697.
7. Desideri, J. A., and Dervieux, A., "Compressible Flow Solvers Using Unstructured Grids", VKI Lecture Series 1988-05, March 7-11, 1988, pp. 1-115.
8. Barth, T. J., and Jespersen, D. C., "The Design and Application of Upwind Schemes on Unstructured Meshes", AIAA-89-0366, Jan. 9-12, 1989.
9. Mavriplis, D.J., Jameson, A., Martinelli, L., "Multigrid Solution of the Navier-Stokes Equations on Triangular Meshes," ICASE Report 89-11, February 1989.
10. Morgan, K., Periare, J., and Peiro, J., "Unstructured Grid Methods for Compressible Flows," AGARD Report R-787, ISBN 92-835-0671-5, May 1992.
11. Löhner, R., "Finite Element Methods in CFD," AGARD Report R-787, ISBN 92-835-0671-5, May 1992.
12. Batina, J. T., "Three-Dimensional Flux-Split Euler Schemes Involving Unstructured Meshes," AIAA Paper No. 90-1649, January 1990.
13. Frink, N.T. "Upwind Scheme for Solving the Euler Equations on Unstructured Tetrahedral Meshes," Paper presented at workshop entitled: "Accuracy of Unstructured Grid Techniques," NASA Langley R.C., January, 1990.
14. Shakib, F., "Finite Element Analysis of the Compressible Euler and Navier-Stokes Equations", PhD Thesis, Department of Mechanical Engineering, Stanford University, 1988.
15. Barth, T.J., "Numerical Aspects of Computing Viscous High Reynolds Number Flows on Unstructured Meshes," AIAA paper 91-0721, January, 1991.
16. Barth, T. J., and Frederickson, P. O., "Higher Order Solution of the Euler Equations on Unstructured Grids Using Quadratic Reconstruction", AIAA-90-0013, Jan. 8-11, 1990.
17. Vankeirsbilck, P., and Deconinck, H., "Higher Order Upwind Finite Volume Schemes with ENO-Properties for General Unstructured Meshes," AGARD Report R-787, ISBN 92-835-0671-5, May 1992.
18. Godunov, S. K., "A Finite Difference Method for the Numerical Computation of Discontinuous Solutions of the Equations of Fluid Dynamics", Mat. Sb., Vol. 47, 1959.
19. Roe, P.L., "Approximate Riemann Solvers, Parameter Vectors, and Difference Schemes", J. Comput. Phys., Vol 43, 1981.
20. Van Leer, B., "Towards the Ultimate Conservative Difference Scheme. IV. A New Approach to Numerical Convection", JCP, Vol. 23, 1977, pp. 276-299.
21. Van Leer, B., "Upwind-Difference Methods for Aerodynamic Problems Governed by the Euler Equations," Lecture Notes in Applied Mathematics, Vol. 22, 1985.
22. Barth, T.J., "A Three-Dimensional Upwind Euler Solver for Unstructured Meshes," AIAA paper 91-1548, Honolulu, Hawaii, 1991.
23. Powell, K.G., Barth, T.J., and Parpia, I.H., "A Solution Scheme for the Euler Equations Based on a Multi-Dimensional Wave Model," AIAA paper 93-0065, Reno, NV, 1993.
24. Valarezo, W.O., Dominik, C.J., and McGhee, R.J., "Multi-Element Airfoil Optimization for Maximum Lift at High Reynolds Numbers," AIAA Paper 91-3332, September, 1991.
25. Baldwin, B.S., and Barth, T.J., "A One-Equation Turbulence Transport Model for High Reynolds Number Wall-Bounded Flows," NASA TM-102847, August 1990.